Microstructure, precipitate and property evolution in cold-rolled Ti-V high strength low alloy steel

Zhang, Xukai; Loannidou, Chrysoula; ten Brink, Gert H.; Navarro-Lopez, Alfonso; Wormann, Jan; Campaniello, Jean; Dalgliesh, Robert M.; van Well, Ad A.; Offerman, S. Erik; Kranendonk, Winfried

Published in:
Materials & design

DOI:
10.1016/j.matdes.2020.108720

Publication date:
2020

Materials and Design 192 (2020) 108720

Contents lists available at ScienceDirect

Materials and Design

journal homepage: www.elsevier.com/locate/matdes

Microstructure, precipitate and property evolution in cold-rolled Ti-V high strength low alloy steel

Xukai Zhang [a,*], Chrysoula Ioannidou [b], Gert H. ten Brink [a], Alfonso Navarro-López [b], Jan Wormann [c], Jean Campaniello [c], Robert M. Dalgliesh [d], Ad A. van Well [e], S. Erik Offerman [b], Winfried Kranendonk [c], Bart J. Kooi [a,*]

[a] Zernike Institute for Advanced Materials, University of Groningen, Nijenborgh 4, 9747AG Groningen, the Netherlands
[b] Department of Materials Science and Engineering, Delft University of Technology, Mekelweg 2, 2628 CD, Delft, the Netherlands
[c] Tata Steel, P.O.Box 10.000, 1970 CA IJmuiden, the Netherlands
[d] STFC, ISIS, Rutherford Appleton Laboratory, Chilton, Oxfordshire OX11 0QX, United Kingdom
[e] Department of Radiation Science and Technology, Delft University of Technology, Mekelweg 15, 2629 JB Delft, the Netherlands

HIGHLIGHTS

- Precipitate evolution was quantitatively characterized by three different state-of-the-art techniques.
- Composition and lattice parameter change of ternary precipitates as function of radius was obtained in the 1-15 nm range.
- Matrix dissolution allowed separate volume fraction determination of three types of precipitates with different size ranges.
- Precipitate volume fractions obtained by matrix dissolution are slightly better than those by small angle neutron scattering.

GRAPHICAL ABSTRACT

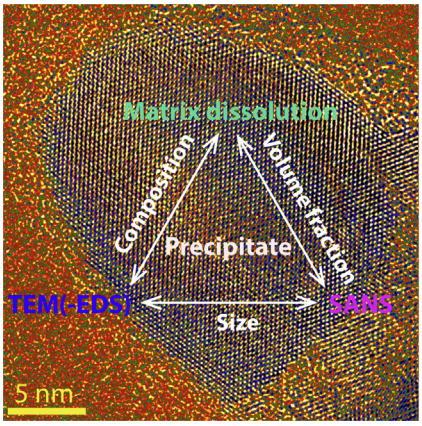

ARTICLE INFO

Article history:
Received 23 February 2020
Received in revised form 24 March 2020
Accepted 5 April 2020
Available online 7 April 2020

Keywords:
Precipitate
Titanium-vanadium-carbide
High strength low alloy steel
Transmission electron microscopy
Small angle neutron scattering
Matrix dissolution

ABSTRACT

A cold-rolled Ti-V high strength low alloy (HSLA) steel was isothermally annealed at 650 °C and 700 °C for different times. A unique combination of techniques including visible light microscopy (VLM), transmission electron microscopy (TEM), matrix dissolution, small angle neutron scattering (SANS) and hardness measurement has been employed to investigate the evolution of microstructure, hardness and precipitate composition, size and volume fraction. Results show that recrystallization is completed after annealing 8 h at 650 °C and 30 min at 700 °C. Three types of precipitates were identified: large Ti(C,N), medium-size (Ti,V)(C,N) and small (Ti,V)C. The Ti/(Ti+V) atomic ratio in the (Ti,V)C precipitates decreases with increasing radius in the 1–15 nm range, which can be explained by the initial nucleation of a TiC-rich core. The average size of the (Ti,V)C precipitates increases, whereas the number density decreases during annealing. The volume fractions of the three types of precipitates were separately determined by the matrix dissolution method. The volume fractions of (Ti,V)C precipitates obtained by matrix dissolution are comparable even slightly more accurate than those obtained by

* Corresponding authors.
E-mail addresses: x.zhang@rug.nl (X. Zhang), b.j.kooi@rug.nl (B.J. Kooi).

https://doi.org/10.1016/j.matdes.2020.108720

SANS. The hardness first increases and then decreases when annealing at both temperatures, which can be correlated well with the observed microstructural and precipitate evolution.

1. Introduction

To reduce energy consumption and CO_2 emission in the past few decades, there has been an increasing demand for lightweight vehicles [1]. Cold-rolled and annealed high strength low alloy (HSLA) steels are widely used in automotive industry to reduce vehicle weight. They are economically favourable, show good weldability and coatability due to their low carbon and low alloy contents and exhibit excellent formability due to the predominant soft ferrite microstructure (the rest is a small amount of pearlite microstructure) [2,3]. However, the low carbon and low alloy contents also result in insufficient strengthening by solid solution and secondary phase hardening. The main active strengthening mechanisms in HSLA steels are due to grain refinement and precipitation hardening, both of which are achieved by nanoscale precipitates containing e.g. niobium (Nb), titanium (Ti), vanadium (V), molybdenum (Mo) individually or in certain combinations [4–7]. These carbides not only increase strength by precipitation hardening [4,5,8], but also retard recrystallization, leading to smaller grain sizes [9,10].

Previous investigations carried out on cold-rolled steels mainly focused on microstructure evolution, mechanical property and recrystallization behavior during annealing [11–17], whereas precipitation behavior received little attention. Since precipitates play a crucial role in determining the final microstructure and mechanical properties, it is necessary to quantitatively assess precipitate size, composition and volume fraction evolution during annealing.

Cold-rolled and annealed HSLA steels micro-alloyed with the elements Ti and V have proven to be promising candidates for products with enhanced performance and low costs, meeting the requirements of CEN Grade HC460LA [3]. Ti is industrially favored not only because of the precipitation hardening and grain refinement, but also due to its relatively low cost. Perrard et al. [18] claimed that vanadium is an ideal micro-alloying element in the cold-rolled and annealed steels from the production point of view. A cold-rolled Ti-V ultra-low carbon steel also exhibit higher yield strength, ductility and deep drawability compared to the steel only containing Ti after annealing at 780 °C [6]. The precipitates formed during annealing in Ti-V steels were identified as spherical (Ti,V)C precipitates with a mean size of several nanometers [6,15,19,20], having a NaCl–type crystal structure and Baker-Nutting orientation relationship of $(100)_{(Ti,V)C}//(100)_{ferrite}$, $[011]_{(Ti,V)C}//[001]_{ferrite}$ with the BCC ferrite matrix [20]. They nucleate and grow on both dislocations and grain boundaries [15]. However, detailed investigations on precipitation behavior, for instance, composition evolution and precipitation kinetics, are lacking.

TEM-based techniques have been frequently used to characterize nanoscale precipitates [3–5,19–30]. Precipitate morphology, size, spatial distribution and volume fraction can be obtained with TEM images and its chemical information can be measured by TEM- energy dispersive X-ray spectroscopy (EDS) or electron energy-loss spectroscopy (EELS).

The matrix dissolution method has been employed to obtain precipitate composition and volume fraction. Samples were dissolved by chemicals [8,31–33] or electrolytes [32,34,35], and filtered with filter papers. Inductively coupled plasma - optical emission spectroscopy (ICP-OES) [31,33], inductively coupled plasma - mass spectroscopy (ICP-MS) [8,32] and inductively coupled plasma - atomic emission spectroscopy (ICP-AES) [34,35] have been employed to determine the element concentrations in the matrix and thus the precipitate volume fraction. It is obvious that the precipitate volume fraction is then underestimated because all precipitates smaller than the filter size are included (erroneously) as part of the matrix. Recently, Lu et al. [32] has shown that centrifuging is a promising alternative for filtering. Precipitates down to 2 nm were successfully separated from the solution after centrifuging and the precipitate volume fraction was derived based on the ICP-MS results in a Nb-Ti micro-alloyed steel. However, the accuracy of this method is unclear, because the centrifuging efficiency is unknown and small precipitates can also dissolve during matrix dissolution.

SANS is a non-destructive method to quantitatively measure size distribution, number density and volume fraction of precipitates ranging from 1 nm to 100 nm [36]. It has been employed to quantify VC [26,27], (Ti, Mo)C [28] interphase precipitates in micro-alloyed steels, NbC precipitates [29] in a α-Fe-Nb-C steel, NbN platelets [30] in a Fe-Nb-N steel, and MnS precipitates [37] in a low carbon steel.

Taking the current status of the field as described above as the starting point, the aim of the present work is twofold: (1) To provide an in-depth understanding of precipitation behavior and microstructure and mechanical property evolution in cold-rolled Ti-V HSLA steels. To do so, the investigated samples were isothermally annealed at 650 °C and 700 °C for different times (Fig. 1a). (2) To test and compare accurate quantification methods of precipitate composition, size and volume fraction. To do so, precipitate compositions have been obtained by TEM-EDS and ICP-OES, precipitate size (distribution) has been obtained by TEM and SANS measurements and finally the precipitate volume fraction has been obtained by SANS and matrix dissolution (Fig. 1b). In the case of matrix dissolution we combined for the first time filtering with centrifuging, increasing the accuracy of this method and obtaining separate volume fraction of precipitates with different size ranges.

2. Experimental

The cold-rolled Ti-V HSLA steel investigated in this work was provided by Tata Steel, IJmuiden. The exact chemical composition of the steel is known, but here only composition ranges for the most relevant elements (wt%) are shown (Table 1). The steel was hot rolled, coiled below 600 °C, followed by cold rolling to the final thickness of 1.5 mm. Cold-rolled samples with dimensions of $10 \times 10 \times 1.5$ mm^3 were isothermally annealed at 650 °C for 2 min, 6 min, 15 min, 30 min, 1 h, 2 h, 8 h and at 700 °C for 1 min, 3 min, 8 min, 15 min, 30 min, 1 h and 4 h (Fig. 1a) with a Bähr 805 A/D dilatometer under a vacuum of 10^{-4} mbar, followed by argon gas cooling to room temperature. An S-type thermocouple was spot-welded to the center of all samples to measure and control the temperature. In the following, the cold-rolled sample is written as “the CR sample”, and annealed samples are named according to their annealing temperature and time, for instance, the sample annealed at 700 °C for 4 h is written as “the 700 °C 4 h sample”.

Samples were hot mounted, ground to one quarter depth and polished with standard procedures. Vickers hardness measurements were performed with a Leitz Wetzlar hardness tester. At least 5 different sample locations were tested for each sample with a load of 200 g for 30 s. 3% Nital solution was used to etch the sample surface after final polishing and microstructures were investigated with an Olympus VANOX-T visible light microscope.

TEM samples were prepared by carbon replica extraction. The well-polished samples were lightly etched with 3% Nital solution before being placed into a carbon coater for depositing a layer of carbon with a thickness of around 5 nm. After carbon deposition, samples were etched in 3% Nital solution for several minutes until the carbon film

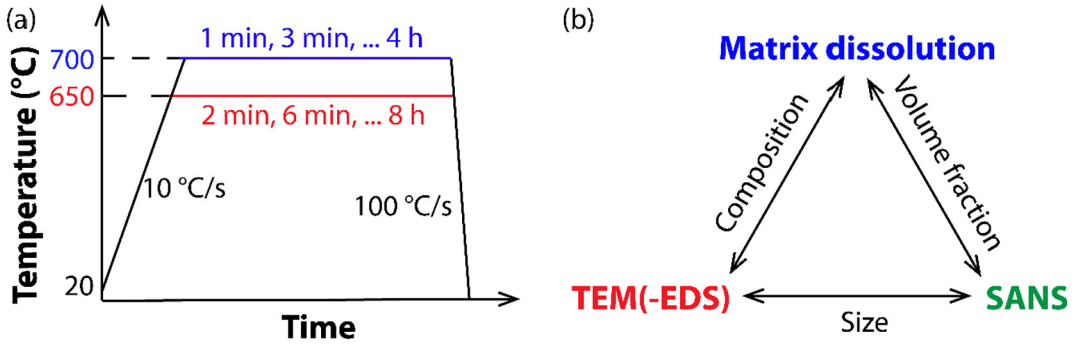

Fig. 1. (a) Schematic annealing procedure for the Ti-V HSLA steel samples, (b) precipitate size (distribution), composition and volume fraction are obtained by pairs of techniques including TEM imaging, TEM-EDS, matrix dissolution combined with ICP-OES and SANS.

started to detach from the steel surface. Nickel (Ni) TEM grids were used to pick up the carbon replicas. TEM investigations were conducted using a JEOL 2010 (a 200 kV TEM equipped with a LaB_6 electron source) and an FEI Themis Z (double aberration corrected TEM and STEM which is equipped with two large race-track EDS detectors (Dual X system), operated at 300 kV for the present work). Image-Pro Plus software was used to measure precipitate radius from bright-field TEM images. 300–500 precipitates were analyzed in each measured sample. An FEI Nova NanoSEM650 scanning electron microscope (SEM) equipped with a high angle annular dark field (HAADF) detector and stitching function was used to investigate the (non-uniform) spatial distribution of precipitates on carbon replicas at 30 kV.

Matrix dissolution experiments were performed on the CR sample and samples annealed at 700 °C for 1 min, 8 min, 1 h and 4 h. In the present work, matrix dissolution refers to the whole process, i.e., chemical dissolution, filtering, centrifuging and ICP-OES measurements. The schematic diagram of matrix dissolution is shown in Fig. S1 (see Supplementary material (SM) Section S1). After weighing the sample (the dimension is about $10 \times 10 \times 1.5$ mm^3) using an analytical balance with an accuracy of 0.1 mg, 12 ml HCl acid solution (1:1 mixture by volume of distilled water and HCl acid with a density of 1.19 g/cm^3 [32]) was used to dissolve the steel matrix at 55 °C. In order to separate precipitates from the solution, vacuum filtration with a 20 nm pore size filter was first conducted, followed by centrifuging performed with a Beckman Coulter Avanti-20 XP. The solution after filtering was quickly rotated up to 21,500 rpm at 4 °C and held for 50 min. ICP-OES measurements were conducted on the supernatant obtained after filtering of the CR sample and after both filtering and centrifuging for all samples to determine the Ti and V concentrations.

SANS experiments were performed at room temperature on the Larmor Instrument at ISIS Neutron and Muon Source (STFC Rutherford Appleton Laboratory). Sample dimensions for the SANS measurements are $10 \times 10 \times 1$ mm^3 (each side of the 1.5 mm steel plate was ground away by 0.25 mm). A 5×5 mm^2 neutron beam and a wavelength range of 0.42–1.33 nm are used. A 3473-70 GMW electromagnet is used to generate a transversal magnetic field of 1.65 T, perpendicular to the neutron beam. This strong magnetic field is necessary to magnetically saturate the specimens, to avoid any contribution to the scattering signal from magnetic domains, and separate the nuclear and magnetic scattering contribution from the SANS pattern [26]. Exposure time of each sample was 25 min.

Table 1
Chemical composition ranges for the most relevant elements of the HSLA steel (wt%).

C	Mn	N	Ti	V
0.03–0.07	0.8–1.2	0.002–0.006	0.03–0.08	0.05–0.12

3. Results

3.1. Visible light microscopy

Micrographs of the CR sample and some samples annealed at 650 °C and 700 °C for different times are shown in Fig. 2. The microstructure in the CR sample contains elongated grains (Fig. 2a). When annealing at 650 °C for 2 min, some sub-grains are observed on the boundaries of deformed grains (Fig. 2b). With the increase of annealing time at 650 °C, the sub-grains continuously form and grow (Fig. 2c) until 8 h, when the recrystallization is nearly finished (Fig. 2d). In comparison, the recrystallization is nearly completed after annealing at 700 °C for 30 min (Fig. 2e). From 30 min to 4 h, grain growth is observed (Fig. 2e and f). Clearly, the recrystallization process in samples annealed at 700 °C is much faster than that at 650 °C.

3.2. Electron microscopy

Bright-field TEM images with precipitates extracted from the CR and 700 °C 4 h samples are shown in Fig. 3a–b and c–d, respectively. Three types of precipitates can be discerned (marked with red arrows) in both samples (in fact in all samples) and their EDS spectra are shown in Fig. 3e. Type I precipitates are large cuboidal titanium-carbonitride (Ti(C,N)) precipitates with sizes between 150 nm and 500 nm (Fig. 3a, c and e). Type II precipitates are medium-size titanium-vanadium-carbonitride ((Ti,V)(C,N)) precipitates ranging from 30 nm to 70 nm with ellipsoidal shape (Fig. 3a, c and e). Type III precipitates comprise small spherical titanium-vanadium-carbide ((Ti, V)C) precipitates with sizes down to 1 nm (Figs. 3b, d and e).

In the EDS spectra in Fig. 3e Ni is present because of the nickel TEM grids. The Fe signal in the EDS spectra probably originates from residual Fe atoms attached on the carbon replicas or from the interphase boundary between the precipitates and the matrix, which was found to be enriched with Fe atoms for (V, Fe)C precipitates in steel in a previous atom probe tomography (APT) study [26].

Similar precipitate types, sizes and compositions have also been reported in a V-Nb-Ti micro-alloyed steel [38]. Type I Ti(C,N) precipitates are believed to form during casting and type II (Ti,V)(C,N) precipitates are believed to form during hot rolling based on the Thermo-Calc simulation in a Ti-V micro-alloyed steel [39]. Both these two types of precipitates are thought to be thermodynamically stable in ferrite and therefore do not change during annealing [38], which is also verified by the present TEM investigations (cf. Fig. 3a and c). In contrast, type III (Ti,V)C precipitates evolve during annealing (cf. Fig. 3b and d). The small amount of (Ti,V)C precipitates observed in the CR sample originates from the coiling process.

Fig. 4a–c show type III (Ti,V)C precipitates in the 700 °C 8 min, 650 °C 30 min and 650 °C 8 h samples, respectively. They all have spherical shape and their size increases with increasing annealing time. Fig. 4d

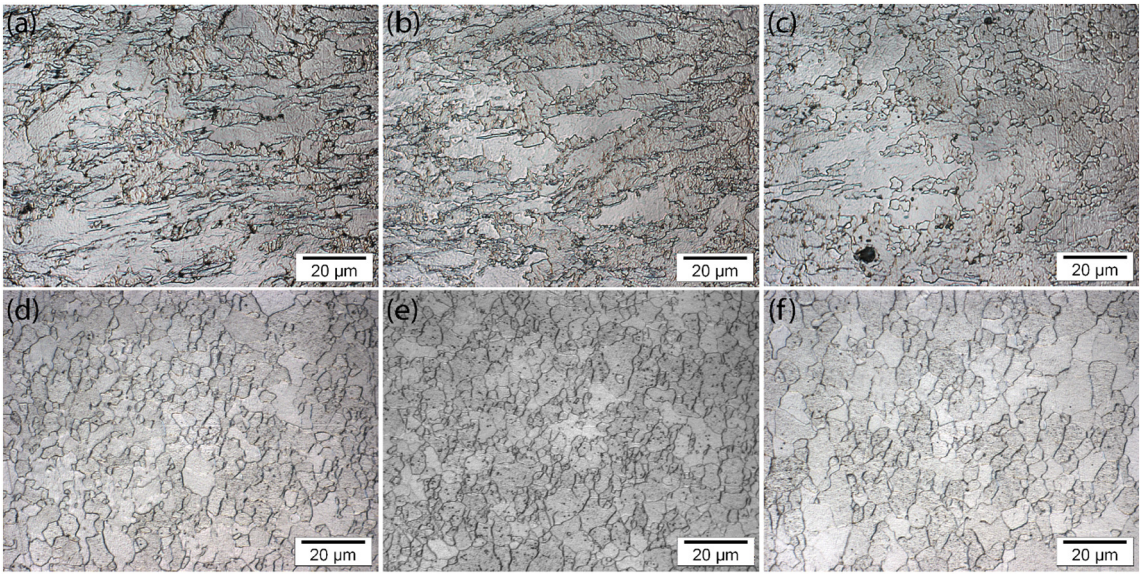

Fig. 2. Micrographs of the samples (a) CR, (b) 650 °C 2 min, (c) 650 °C 2 h, (d) 650 °C 8 h, (e) 700 °C 30 min and (f) 700 °C 4 h.

shows size distributions of the (Ti,V)C precipitates and their corresponding lognormal fits as derived from a large number of TEM images (300–500 precipitates) of the 650 °C 30 min, 650 °C 8 h, 700 °C 8 min and 700 °C 4 h samples. The median radius increases with increasing annealing time and temperature. Particularly for the longest annealing times at 650 °C and 700 °C precipitate coarsening can be observed. It is worth noting that precipitates with radius smaller than 0.5 nm cannot be distinguished in the TEM images and the precipitates between 0.5 nm and 1 nm are underestimated due to the noisy carbon background. Therefore, the provided values in this range in Fig. 4d are lower than the real ones.

Fig. 4e shows the Ti/(Ti + V) atomic ratio of the (Ti,V)C precipitates (obtained from EDS measurements) as a function of precipitate radius in the 650 °C 8 h, 700 °C 8 min and 700 °C 4 h samples. The Ti/(Ti + V) atomic ratio decreases with the increase of precipitate radius. The ratios are almost the same as a function of radius for the 700 °C 8 min and 4 h samples, indicating that the Ti/(Ti + V) atomic ratio is not time dependent. Similarly, there is no observable difference for the Ti/(Ti + V) atomic ratio between the 700 °C 4 h and 650 °C 8 h samples. This also agrees with the Thermo-Calc simulation, which shows that the Ti/(Ti + V) atomic ratio of equilibrium (Ti,V)C precipitates is nearly the same at 650 °C and 700 °C [39]. When the trend observed in the experimental data in Fig. 4e is extrapolated down to a nucleus with 0.5 nm radius, the Ti/(Ti + V) atomic ratio reach values in the range 0.7–1, indicating that the initial nucleus must have a TiC-rich core.

Summarizing information on the three types of precipitates is given in Table 2.

Fig. 5a and b show high resolution TEM (HRTEM) images of a 9.3 ± 0.9 nm (Ti,V)C precipitate. The corresponding fast Fourier transform (FFT) shown in Fig. 5c indicates that viewing is along the [011] zone axis. Fig. 5d and e show the HRTEM image and FFT of a 1.9 ± 0.2 nm (Ti,V)C precipitate as viewed along the [001] zone axis, respectively. Precipitate plane distances in Fig. 5b and d were calculated based on the reciprocal distances in Fig. 5c and e, respectively. The slight differences between the two sets of {111} planes in Fig. 5b and the two sets of {200} planes in Fig. 5d can be the result of a slight crystal tilt (away from zone axis).

It is reasonable to assume that the lattice parameter of (Ti,V)C can be estimated by linear interpolation between the ones of TiC and VC because (Ti,V)C has the same crystal structure as pure TiC and VC and Ti and V appear perfectly miscible on their sub-lattice. The theoretical lattice parameter of $(Ti_xV_{1-x})C$ precipitates can then be expressed as:

$$a_{(Ti_xV_{1-x})C} = x \cdot a_{TiC} + (1-x) \cdot a_{VC} \quad (1)$$

where a_{TiC} and a_{VC} are the lattice parameters of TiC and VC, with values of 0.4367 nm and 0.4187 nm, respectively [40].

Fig. 5f shows the theoretical lattice parameter of the (Ti,V)C precipitates as a function of precipitate radius based on the Ti/(Ti + V) atomic ratio obtained from EDS measurements and three experimental values obtained from FFT of the HRTEM images. The lattice parameter of the experimental and theoretical values agree well with each other, both decreasing with increasing precipitate radius.

A stitched HAADF-STEM image taken with a SEM demonstrates that type III (Ti,V)C precipitates are not uniformly distributed (see Fig. S2 in SM Section S2). Their distribution suggests that bigger (Ti,V)C precipitates are present on grain boundaries whereas smaller (Ti,V)C precipitates nucleate on dislocations inside the grains. This is consistent with the work in [15], in which big (Ti,V)C precipitates at grain boundaries were illustrated with a bright-field STEM image and EDS chemical mapping. The result makes it obvious that it is not accurate to derive the precipitate volume fraction from small volumes and thus excludes techniques like TEM or atom probe tomography (APT). In contrast, matrix dissolution or SANS is then much more suitable.

3.3. Matrix dissolution

Since three types of precipitates with different size ranges are present in the current steel, a filtering procedure with 20 nm filter paper was added between chemical dissolution and centrifuging compared with the steps described by Lu et al. [32].

In order to fully trust the current matrix dissolution method, two main issues have to be addressed. The first one is the centrifuging efficiency. Centrifuging directly after chemical dissolution shows that big clusters of precipitates cannot stick to the wall of the centrifuging tube and go back into solution again. This problem is solved by filtering with 20 nm pore size filter before centrifuging, which guarantees an efficient precipitate separation from the matrix. Sediments after centrifuging and solutions both before and after centrifuging with the same dilution were examined with TEM (see SM Section S3). The results indicate that the centrifuging efficiency is high enough to generate a sufficiently accurate precipitate volume fraction. The second issue is the potential dissolution of the precipitates. It was reported that NbC and

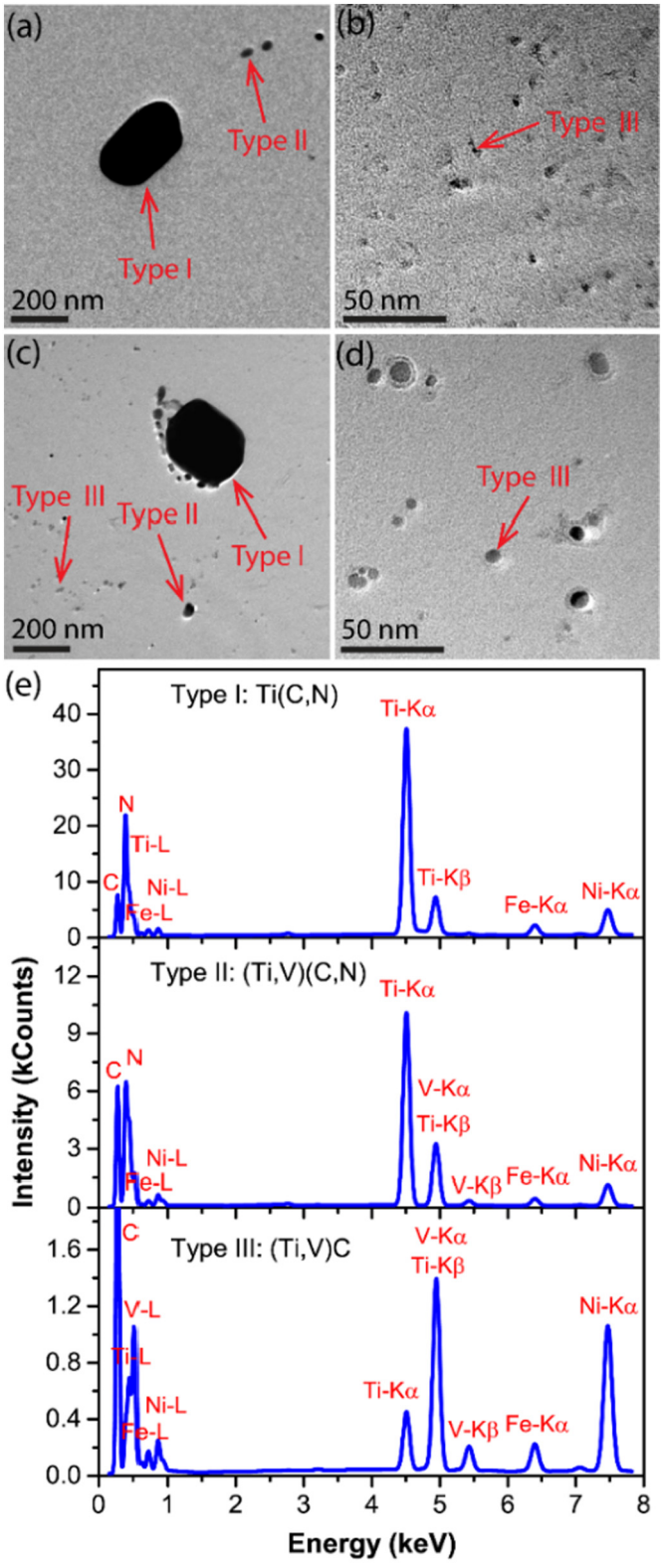

Fig. 3. Representative examples of bright-field TEM images of carbon replicas showing sizes and morphologies of the three different types of precipitates in the sample (a), (b) CR, (c), (d) 700 °C 4 h, and (e) EDS spectra of the three types of precipitates.

NbN do not dissolve in HCl solution, and then it can be expected that this also holds for carbides and nitrides that contain Ti and V, because they have the same crystal structure and stability [32]. However, it is better to directly test this expectation experimentally. We therefore dissolved pure VC particles with a diameter of about 2 μm in HCl solution and found that not >1.1% of the VC particle mass dissolved (see SM Section S4), demonstrating that precipitate dissolution is limited. However, the dissolution rate of 2 μm particles is definitely smaller than particles of several nanometers. Nevertheless, the results of the experiments described below, including the comparison with the SANS results, will demonstrate that even these small precipitates hardly dissolve.

ICP-OES measurements were first performed on the supernatant after only filtering the dissolved CR sample. In this way, the Ti and V concentrations in the matrix and the type III (Ti,V)C precipitates were obtained. By subtracting these concentrations from the known overall concentrations, the Ti and V concentrations in the type I Ti(C,N) and type II (Ti,V)(C,N) precipitates were determined. Based on the Ti/(Ti + V) atomic ratio in these two types of precipitates, the Ti and V concentrations in each type of precipitate can be calculated. For the other annealed samples, it is assumed that Ti(C,N) and (Ti,V)(C,N) precipitates do not change. Next, ICP-OES measurements were performed for the supernatants of all samples after both filtering and centrifuging each sample. Ti and V concentrations in the matrix of all samples were obtained in this way. The Ti and V concentrations in type III (Ti,V)C precipitates were obtained since the Ti and V concentrations in Ti(C,N), (Ti,V)(C,N) precipitates and in the matrix have been determined and can be subtracted from the known overall concentrations.

Fig. 6a and b show the percentage of the Ti and V to the total amount in the three types of precipitates in the CR sample and samples annealed at 700 °C for 1 min, 8 min, 1 h and 4 h, respectively. For Ti(C,N) and (Ti,V)(C,N) precipitates together, they have consumed 40.2% of the total amount of Ti and only 0.6% of the total amount of V, resulting in the Ti/(Ti + V) atomic ratio of 0.969. For (Ti,V)C precipitates, 4.4% of the total amount of V has precipitated out in the CR sample and increased to 78.5% after annealing at 700 °C for 4 h. Ti concentration in (Ti,V)C precipitates is very low in the CR sample and rises to 53.7% after 4 h annealing at 700 °C. Fig. 6c shows the average Ti/(Ti + V) atomic ratio of (Ti,V)C precipitates, indicating a slight decrease with increasing annealing time. The small difference between 1 min and 4 h (0.270 ± 0.017 for 1 min and 0.251 ± 0.002 for 4 h) agrees well with TEM-EDS results (cf. Fig. 4e), which show that the Ti/(Ti + V) atomic ratio of (Ti,V)C precipitates in the 700 °C 8 min and 700 °C 4 h samples is nearly the same.

Combining Eqs. (S1)–(S6) (see SM Section S5), the volume fractions of the three types of precipitates were calculated and are shown in Fig. 6d. The total volume fraction of type I Ti(C,N) and type II (Ti,V)(C,N) precipitates combined is 0.038 ± 0.002%, of which 0.023 ± 0.007% is Ti(C,N) and 0.015 ± 0.007% is (Ti,V)(C,N). The volume fraction of type III (Ti,V)C precipitates for the CR sample is 0.011 ± 0.006%. It increases with increasing annealing time, reaching 0.189 ± 0.003% for the 700 °C 4 h sample.

3.4. SANS

The initial output of SANS measurements is a 2D scattering pattern. It was transformed into 1D data following the methods described in [26], giving the relationship between differential scattering cross-section $d\Sigma/d\Omega$ and scattering vector Q. It consists of two parts: nuclear scattering $(d\Sigma/d\Omega)_{NUC}$ and magnetic scattering $(d\Sigma/d\Omega)_{MAG}$. In the present work, nuclear scattering data, obtained by considering the sectors of 30° parallel to the magnetic field, was used for precipitate analysis. The SANS signal from the CR sample (with pre-existing precipitates and dislocations) is used as background signal for the other annealed samples. Therefore, only precipitates formed during annealing, i.e., type III (Ti,V)C precipitates in annealed samples are quantitatively characterized.

Based on the expression of nuclear differential scattering cross-section of precipitates surrounded by a homogenous matrix in a dilute system [41,42] and taking into consideration precipitate composition variance with its size, the current nuclear differential scattering cross-

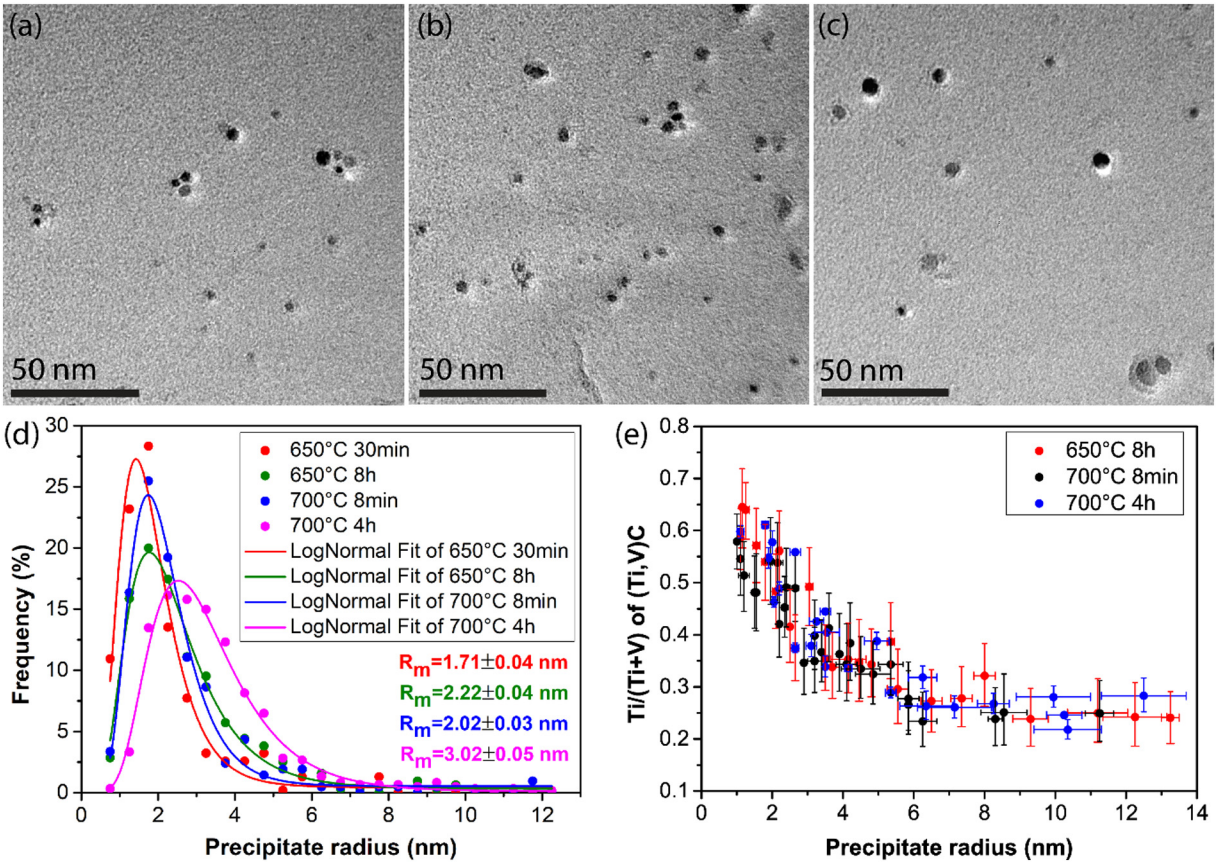

Fig. 4. Representative examples of bright-field TEM images of carbon replicas showing type III (Ti,V)C precipitates in the sample (a) 700 °C 8 min, (b) 650 °C 30 min, (c) 650 °C 8 h, (d) size distributions of (Ti,V)C precipitates and their corresponding lognormal fits as derived from a large number of TEM images (300–500 precipitates) of the 650 °C 30 min, 650 °C 8 h, 700 °C 8 min and 700 °C 4 h samples, (e) Ti/(Ti + V) atomic ratio of the (Ti,V)C precipitates as a function of precipitate radius in the 650 °C 8 h, 700 °C 8 min and 700 °C 4 h samples.

section of precipitates can be written as:

$$\left(\frac{d\Sigma}{d\Omega}\right)_{NUC}(Q) = \int (\Delta\rho_{NUC}(R))^2 D_N(R)\cdot V^2(R)\cdot P^2(Q,R)dR \tag{2}$$

where R is the precipitate radius. $\Delta\rho_{NUC}(R)$ is the difference in nuclear scattering length density of precipitates and $(\Delta\rho_{NUC}(R))^2 = (22.0 + 12.3\cdot R^{-0.44})\times 10^{-8}\ \mathrm{nm}^{-4}$ (see SM Section S6). $V(R)$ and $P(Q, R)$ are the precipitate volume and the form factor that describes precipitate shape, respectively. For spherical (Ti,V)C precipitates, $V(R) = 4/3\pi R^3$ and $P(Q,R) = 3(\sin(QR) - (QR)\cos(QR))/(QR)^3$ [43]. $D_N(R)$ is the product of the precipitate number density N_p and the precipitate lognormal size distribution (according to TEM results in Fig. 4d) and is expressed as:

$$D_N(R) = \frac{N_p}{R\sigma\sqrt{2\pi}}\ exp\left\{-\frac{[\ \ln(R) - \ln(R_m)]^2}{2\sigma^2}\right\} \tag{3}$$

where σ is a parameter of lognormal size distribution (related to the standard deviation and to the mean value) and R_m is the median precipitate radius.

The volume fraction of the precipitates can be calculated by integrating the $Q^2(d\Sigma/d\Omega)_{NUC}$ curve (also known as Kratky plot) for the appropriate Q interval. For a dual-phase system, the area $Q_{o,NUC}$ below the Kratky plot is [26]:

$$Q_{0,NUC} = \int_0^\infty Q^2\left(\frac{d\Sigma}{d\Omega}\right)_{NUC} dQ \approx 2\pi^2(\Delta\rho_{NUC})^2 f_V(1-f_V) \tag{4}$$

Formally $\Delta\rho_{NUC}$ depends (a bit) on R, but performing the integration to obtain the right-hand side of Eq. (4) a constant average is used, based on the average precipitate composition obtained by ICP-OES measurements ($26.33\times 10^{-8}\ \mathrm{nm}^{-4}$ for the average $(\Delta\rho_{NUC})^2$), and therefore the $\approx$ symbol applies. Since the volume fraction of precipitates in steel is very low, Eq. (4) can be simplified to:

$$f_V \approx \frac{Q_{0,NUC}}{2\pi^2(\Delta\rho_{NUC})^2} \tag{5}$$

Table 2
Summary of the three types of precipitates.

Type	Composition	Spectral atomic ratios[a]	Morphology	Size (nm)	Origination	Stability
I	Ti(C,N)	$Ti(C_{0.10}N_{0.90})$	Cuboidal	150–500	Casting	Stable
II	(Ti,V)(C,N)	$(Ti_{0.84}V_{0.16})(C_{0.5}N_{0.5})$ - $(Ti_{0.94}V_{0.06})(C_{0.5}N_{0.5})$	Ellipsoidal	30–70	Hot rolling	Stable
III	(Ti,V)C	$(Ti_{0.70}V_{0.30})C$-$(Ti_{0.20}V_{0.80})C$	Spherical	1–30	Annealing	Evolve

[a] Note: The (Ti + V)/(C + N) ratios of all the three types of precipitates are assumed to be 1 based on APT measurements, which showed that relatively large VC precipitates with a radius of 4 nm have a V:C ratio of 1:1 in the core of the precipitates [26]. The C/(C + N) atomic ratios for type I and II precipitates as derived from EDS measurements are relatively accurate due to their large sizes.

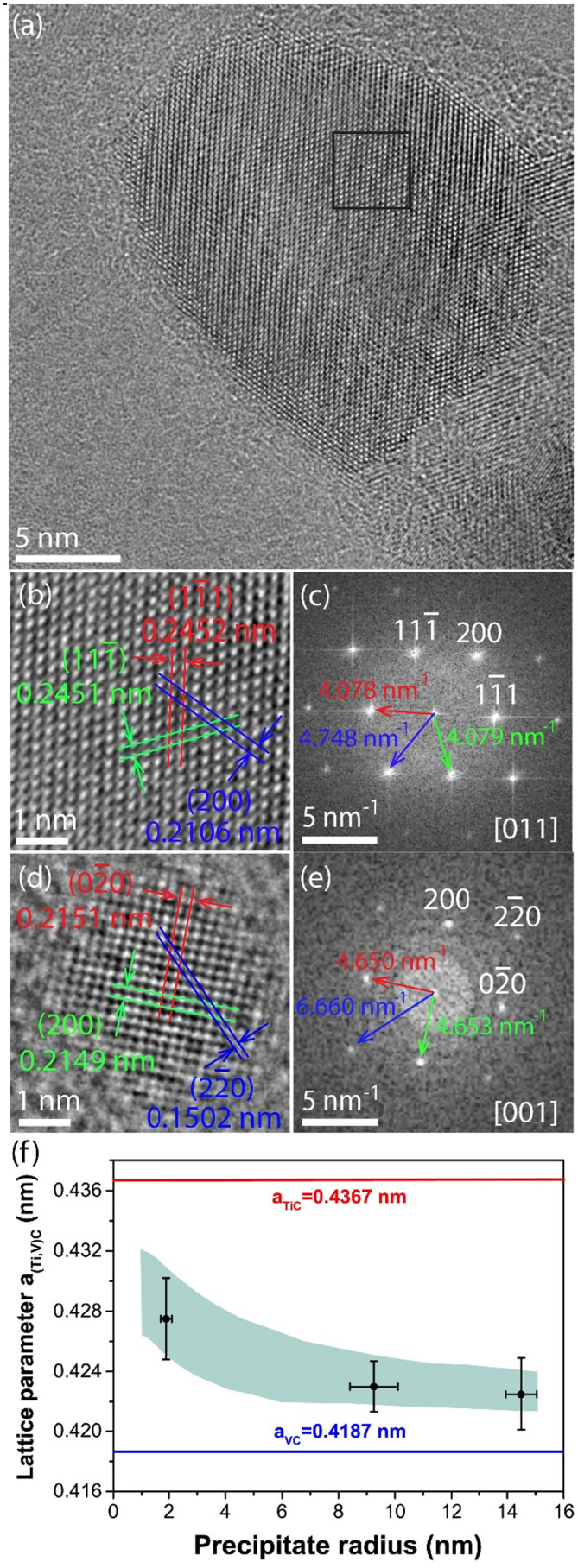

Fig. 7a shows $(d\Sigma/d\Omega)_{NUC}$ as a function of Q for the samples annealed at 650 °C. Compared to the CR sample, the scattering intensity in the 650 °C 2 min sample increases for the whole Q range mainly because of nucleation and growth of small (Ti,V)C precipitates. The scattering intensity drop for $Q < 0.15$ nm^{-1} in the 650 °C 6 min sample is most probably caused by the annihilation of dislocations and sub-grain growth due to recrystallization process, because large objects like grain boundaries, dislocations and large precipitates contribute to scattering intensities at low Q value [41,44]. With the increase of annealing time, the scattering intensity increases for the whole Q range because of precipitate growth. It is obvious that the increase in scattering intensity caused by precipitation is dominant compared with the decrease caused by dislocation annihilation. Fig. 7b shows $(d\Sigma/d\Omega)_{NUC}$ as a function of Q for the samples annealed at 700 °C with a similar scattering intensity evolution trend to that at 650 °C. The scattering intensity drops for $Q < 0.15$ nm^{-1} after annealing for 1 min, indicating a faster dislocation annihilation and sub-grain growth process than at 650 °C.

Fig. 7c and d show the calculated time evolution of $Q^2(d\Sigma/d\Omega)_{NUC}$ as a function of Q after background subtraction of the CR sample for the samples annealed at 650 °C and 700 °C, respectively. The peak shifts towards low Q value, indicating precipitate growth or coarsening. The Kratky plots are fitted by Eq. (2) after it is multiplied by Q^2 (solid lines in Fig. 7c and d), from which fitting parameters of R_m, N_p, σ are obtained. Note here that the fitted curves based on a single lognormal size distribution show deviations from the measured data at low Q values, especially for the 650 °C 8 h, 700 °C 1 h and 700 °C 4 h samples, because of distinct size distributions that hold for smaller (Ti,V)C precipitates inside the grains and bigger (Ti,V)C precipitates on grain boundaries (see Fig. S2). The fitted R_m values should increase with the increase of annealing time, so some fitting involved restricted R_m ranges (the samples annealed at 650 °C for 30 min, 1 h, 2 h and at 700 °C for 8 min, 1 h, 4 h).

Figs. 8a and b show the evolution of precipitate median radius R_m and number density N_p, respectively. The complete size distributions, based on these results and Eq. (3), are shown in Fig. S6. Generally, R_m increases whereas N_p decreases with the increase of annealing time. Due to the large error bar of N_p for the shortly annealed samples, we cannot conclude when the nucleation process finishes. The R_m as obtained by TEM (see Fig. 4d) are bigger than the ones obtained by SANS. This will be explained in Section 4.1.1.

The precipitate volume fraction f_v is calculated by integrating the area under Kratky plot using Eqs. (4) and (5). Following the methods in [26], the integrated area consists of two parts: the area below the experimental Kratky plot in the range of 0.05 nm^{-1} ≤ Q ≤ 1.02 nm^{-1} and the area below the fitted Kratky plot in the range of 1.02 nm^{-1} ≤ Q ≤ 3 nm^{-1}. The precipitate volume fraction is shown in Fig. 8c. It gradually increases, reaching 0.129 ± 0.016% and 0.168 ± 0.018% for the 650 °C 8 h and 700 °C 4 h samples, respectively.

3.5. Hardness evolution

The hardness evolution of the samples annealed at 650 °C and 700 °C is shown in Fig. 9. The hardness of the CR sample is 282.8 ± 6.3 HV. When annealing at 650 °C, the hardness first increases to a maximum value of 304.2 ± 4.2 HV after 6 min, then decreases to 167.6 ± 3.5 HV after 8 h. While at 700 °C, hardness rises to 308.4 ± 5.9 HV after 1 min and drops to 155.1 ± 4.7 HV after 4 h. Precipitation hardening is dominant at the early stage and results in the hardness increase. The higher precipitate volume fraction and median size of the 700 °C

Fig. 5. (a) HRTEM images of a 9.3 ± 0.9 nm (Ti,V)C precipitate, (b) zoom in HRTEM image of the black square in (a), (c) FFT of (b), (d) HRTEM image of a 1.9 ± 0.2 nm (Ti,V)C precipitate, (e) FFT of (d), (f) theoretical lattice parameter of the (Ti,V)C precipitates as a function of precipitate radius based on Ti/(Ti + V) atomic ratio obtained from EDS measurements (cf. Fig. 4d) and three experimental values obtained from FFT of the HRTEM images (cf. Fig. 5c and e).

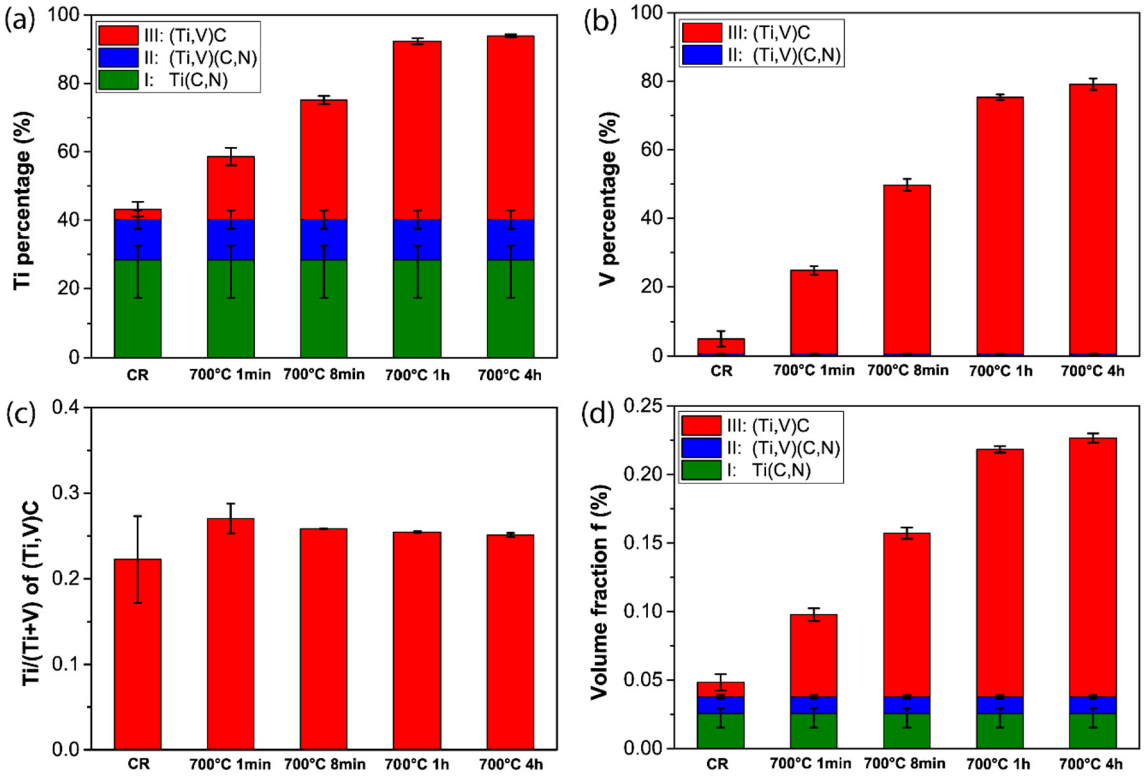

Fig. 6. Results of chemical matrix dissolution, filtering, centrifuging and ICP-OES measurements of the CR sample and samples annealed at 700 °C for 1 min, 8 min, 1 h and 4 h. (a), (b) Ti and V percentage to the total amount in all three types of precipitates, (c) average Ti/(Ti + V) atomic ratio of (Ti,V)C precipitates, (d) volume fractions of the three types of precipitates derived from ICP-OES measurement results. The error bars on (Ti,V)(C,N) in (a) and (d) are actually for (Ti,V)(C,N) and Ti(C,N) together, derived from the ICP-OES results of the filtered CR solution.

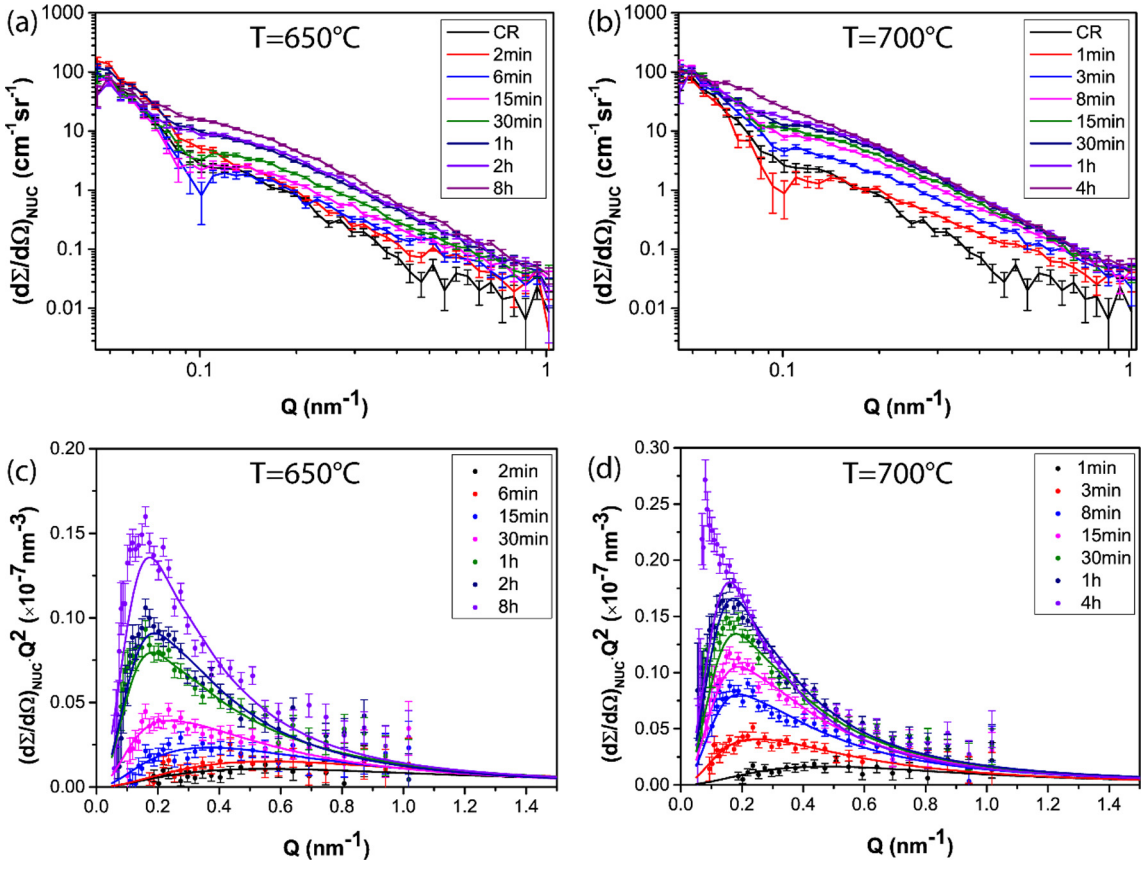

Fig. 7. Time evolution of $(d\Sigma/d\Omega)_{NUC}$ as a function of Q measured at room temperature for samples annealed at (a) 650 °C, (b) 700 °C. Time evolution of $Q^2(d\Sigma/d\Omega)_{NUC}$ as a function of Q after background subtraction of the CR sample for samples annealed at (c) 650 °C, (d) 700 °C, solid lines are the best fits using the model given by Eqs. (2) and (3).

1 min sample leads to the higher hardness peak value than the 650 °C 6 min sample (see Fig. 8a and c).

4. Discussion

4.1. Precipitate quantification methods comparison

Nano-scale precipitates can be quantitatively characterized by TEM-based imaging, TEM-EDS, SANS, matrix dissolution and APT. However, the small volume of a typical APT tip ($15 \times 15 \times 100$ nm^3 [45]) limits statistical analysis of precipitate composition, size, number density and volume fraction. It can only deliver statistically relevant results when the small precipitates are homogeneously dispersed with very high density such that at least tens of precipitates are present in an APT tip. We demonstrated that the precipitates are not uniformly distributed in the matrix (Fig. S2) and the number density is not that high (Fig. 8b). There would be less than one precipitate in an APT tip with the above-mentioned dimensions. Due to the small amount of precipitates analyzed, APT can therefore not provide accurate quantification results for size distribution and volume fraction. Even when the compositions of a few precipitates are determined accurately, then it is still not known how representative these compositions are for other precipitates.

The investigated area in TEM is also small, but since we can still investigate hundreds of precipitates, the precipitate size distribution and compositions can be determined with reasonable accuracy. For instance, when the size distribution is based on ten different bins, a total of hundred analyzed precipitates means that the average number per bin is ten. Then, since Poisson statistics hold, the average accuracy per bin is 10 plus or minus the square root of 10. This already large error bar implies that it is definitely required to analyze at least one hundred precipitates to obtain a reasonably accurate size distribution.

In contrast to APT and TEM, matrix dissolution and SANS investigate a large volume (typically values are both larger than $5 \times 5 \times 10$ mm^3). However, matrix dissolution does not allow determination of the precipitate size distribution. Still the average composition of the precipitates (in different size ranges) and the total precipitation volume fraction can be determined accurately for a large sample volume. SANS in principle allows the assessment of the precipitate size distribution, but this assessment is quite indirect and its accuracy can be debated, because of low signal-to-noise (SN) ratio and since it also heavily relies on modeling with inherent assumptions such as that the size distribution is of lognormal type. On the other hand, the total precipitation volume fraction can be determined accurately using SANS, since this relies on an integrated intensity signal, that inherently possess a larger SN ratio, but also depends much less on modeling assumptions.

4.1.1. Precipitate size

For type III (Ti,V)C precipitates, the median size as obtained by TEM is overestimated because of the underestimation of small precipitates below 1 nm. A systematic error for median precipitate size might be caused by the non-uniform precipitate distribution when the investigated area by TEM is not representative, although 300–500 precipitates were counted in each measured sample. The median size as obtained by SANS is slightly overestimated because of the very small fraction of pre-existing (Ti,V)C precipitates in the CR sample, whose signal is subtracted as background signal in the annealed samples. On the other hand, it is underestimated because the experimental Kratky plots at low Q values (corresponding to bigger precipitate sizes) are not captured by the fitted plots when a single lognormal size distribution is used in Eq. (3). This underestimation becomes obvious with the increase of annealing time because the longer the annealed time the more distinct the precipitate size difference on grain boundaries and inside the grains. As a result, the precipitate median sizes as obtained by SANS is most likely overestimated for the samples with shorter annealing times whereas it is underestimated for the samples with longer annealing times. The above discussions explain why precipitate median sizes as obtained by TEM are higher than those as obtained by SANS in Fig. 8a. This result is consistent with the previous reports that mean sizes obtained by TEM are higher than those obtained by SANS for

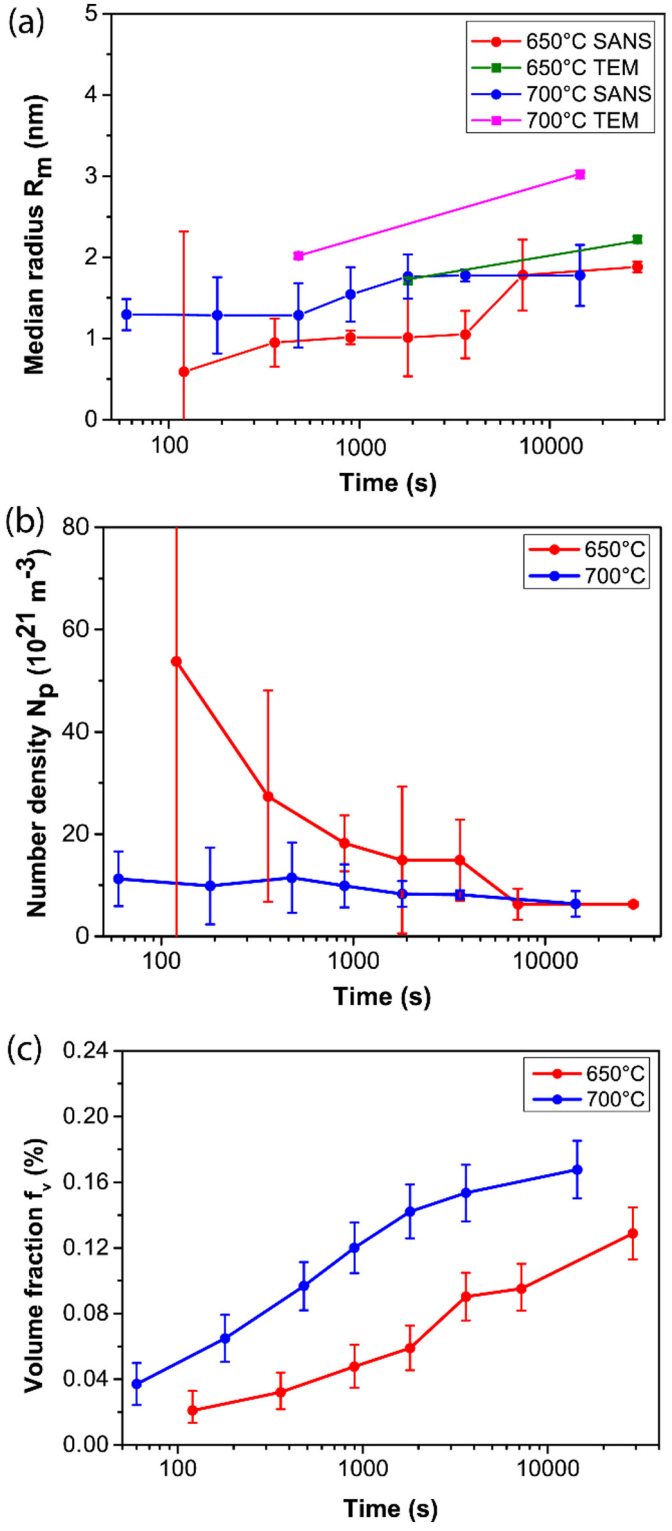

Fig. 8. Evolution of precipitate (a) median radius R_m, (b) number density N_p, (c) volume fraction f_v as derived from SANS measurements of samples annealed at 650 °C and 700 °C. The R_m values, especially for the 650 °C 8 h, 700 °C 1 h and 700 °C 4 h samples are underestimated due to the big (Ti,V)C precipitates on grain boundaries not properly captured in the fits at low Q values in Fig. 7c and d.

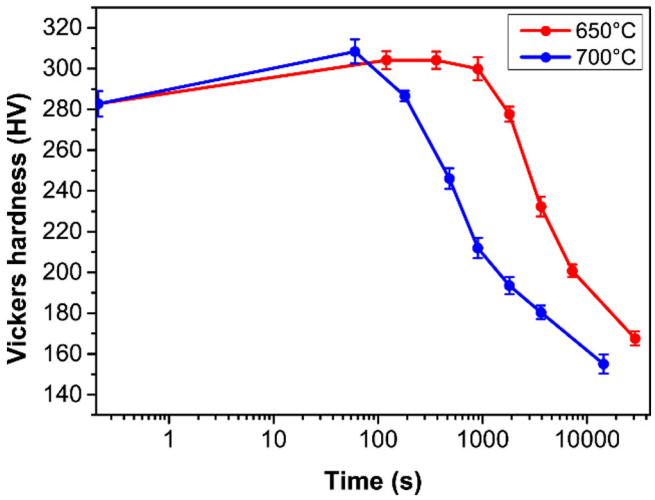

Fig. 9. Hardness evolution in HSLA steel samples isothermally annealed at 650 °C and 700 °C.

precipitates with radius smaller than 5 nm [28,45,46]. For bigger precipitates, results of the two methods agree relatively well [37].

Most (Ti,V)C precipitates investigated by TEM are inside the grains whereas few big (Ti,V)C precipitates formed at grain boundaries are included in the obtained size distribution with TEM (cf. Figs. 4d and S2) due to the small investigated area. The median size as obtained from the SANS measurements is based on the assumption that precipitate size shows a lognormal distribution and precipitates are homogeneously distributed over the volume of the sample. Therefore, both these two methods have difficulty in properly accounting for the precipitates on grain boundaries.

4.1.2. Precipitate composition

The Ti/(Ti + V) atomic ratio of individual precipitates can be obtained by TEM-EDS whereas the average Ti/(Ti + V) atomic ratio determination is impossible. For ICP-OES this is reversed. In this respect, the two techniques are complementary.

For (Ti,V)C precipitates, both TEM and SANS results show that the median radius is between 1 nm and 3 nm. Based on Fig. 4e, the average Ti/(Ti + V) atomic ratio obtained by TEM-EDS should then be between 0.3 and 0.7, which is higher than that obtained by ICP-OES measurements (0.25–0.27). This is mainly because big (Ti,V)C precipitates on the grain boundaries occupy a large volume and play a dominant role in determining with matrix dissolution the average Ti/(Ti + V) atomic ratio. In turn, it proves that precipitate size does not follow the lognormal distribution when precipitates both on grain boundaries and inside the grains are considered.

4.1.3. Precipitate volume fraction

The volume fractions of the three types of precipitates were obtained separately with the matrix dissolution method. In contrast, only the volume fraction of precipitates grown during annealing, i.e. type III (Ti,V)C precipitates, was obtained with the SANS measurements.

The volume fraction of the (Ti,V)C precipitates is underestimated by both the matrix dissolution and the SANS methods. The slight underestimation by matrix dissolution is because precipitates are a bit dissolved and the centrifuging efficiency is not 100%. Whereas the pre-existing small (Ti,V)C precipitates in the reference CR sample and the decrease in dislocation density upon annealing result in small underestimation for SANS measurements. Therefore, the method which gives a higher volume fraction value should be more accurate.

Fig. 10 shows volume fraction comparison of the (Ti,V)C precipitates obtained from matrix dissolution, SANS and SANS+CR. The precipitate volume fractions as obtained by matrix dissolution are a little higher than those directly obtained by SANS for the samples annealed at 700 °C for 1 min, 8 min and 1 h but almost the same for 4 h. Yet, when the volume fraction in the CR sample obtained by matrix dissolution is added to the values obtained by SANS, the SANS+CR and matrix dissolution results agree very well. Therefore, we demonstrate that the matrix dissolution method is quite accurate. The results, in turn, show that the precipitate separation efficiency by matrix dissolution method is high and that the precipitate dissolution must have been limited. The results based on matrix dissolution possess a smaller error compared to the results based on the SANS results.

The present work demonstrates that this modified matrix dissolution method is quite powerful for obtaining precipitate volume fractions in steels. By combining filtering with different pore size filter paper and centrifuging, volume fractions of precipitates with different size ranges, which form during casting, hot rolling and annealing, can be obtained. This is quite important when further analysis is desired, such as verifying thermodynamic simulation results of element fractions in precipitates and the precipitate volume fraction, calculating Zener pinning force and precipitate strengthening because these effects show large differences for precipitates with different sizes [2]. The method proposed here is quite general and can thus be applied to a wide range of steels (or metal alloys) containing precipitates. A crucial requirement for the matrix dissolution method is of course that the matrix can be dissolved, without any appreciable dissolution of precipitates. Summary of appropriate solution recipes for different precipitates and materials can be found in [35,47,48].

4.2. Precipitate evolution

Precipitates nucleated on dislocations inside the grains and on grain boundaries, as deduced from Fig. S2. Based on [49], the change in Gibbs free energy ΔG as a result of precipitation can be expressed as:

$$\Delta G = \begin{cases} V(\Delta g_v + \Delta g_s) + A\gamma + \Delta G_{dis} \text{ (on dislocations)} \\ V(\Delta g_v + \Delta g_s) + A\gamma + \Delta G_{gb} \text{ (on grain boundaries)} \end{cases} \quad (6)$$

where V and A are respectively the volume and the area of the nucleus, Δg_v is the chemical driving force (negative), γ is the interface energy between the precipitate and the matrix, Δg_s is the strain energy (positive) that arises as a result of the difference in volume between the precipitate and the matrix, ΔG_{dis} and ΔG_{gb} are the released energy due to nucleation on dislocations and grain boundaries, respectively. The activation energy for nucleation can be calculated with the critical nucleation radius which is obtained by taking the derivative of ΔG with respect to R. VC has a lower lattice misfit with ferrite matrix compared to TiC and thus potentially less positive Δg_s and γ values. Jang et al. [40] reported a more negative Δg_v value (formation energy is used in [40]) for TiC compared to VC as based on first principle calculations. Since TEM-EDS composition of the (Ti,V)C precipitates agrees with a TiC-rich core (Fig. 4e), this formation energy Δg_v must be dominant. It is of course possible, even likely, that the nucleus is not pure TiC, but with a small amount of V.

After nucleus formation, both V and Ti diffusion are needed for precipitate growth. Precipitate growth and coarsening rates are proportional to the diffusion coefficient [50,51]. The diffusion coefficients for grain boundaries are higher than that for dislocations, and much higher than that for lattices [52]. Therefore, precipitates on grain boundaries grow and coarsen faster than those inside the grains. This difference becomes more obvious with the increase of annealing time because dislocation density decreases. As a result, the precipitates overall do not show a lognormal size distribution. The diffusion coefficient of Ti is lower than that of V [53], also resulting in the observed decrease of the Ti/(Ti + V) atomic ratio in the (Ti,V)C precipitates when they grow bigger. The median size of the (Ti,V)C precipitates reach 2.22 nm after annealing at 650 °C for 8 h and 3.02 nm at 700 °C for 4 h (see

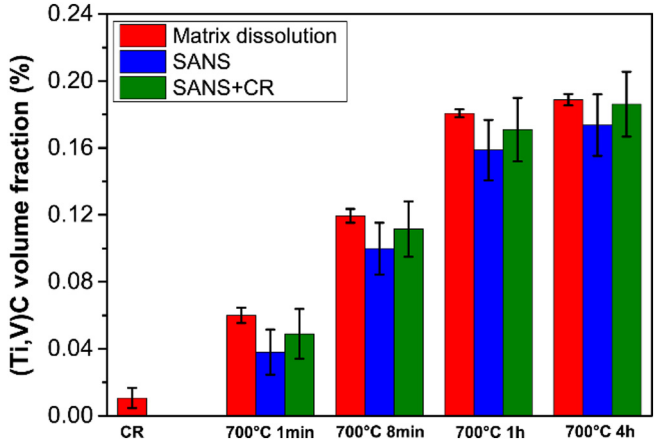

Fig. 10. Volume fraction comparison of (Ti,V)C precipitates obtained from matrix dissolution, SANS and SANS+CR. The "SANS+CR" means that the volume fraction in the CR sample obtained by matrix dissolution is added to the values obtained by the SANS measurements.

Fig. 4d). This growth (coarsening) rate is low. Dunlop et al. [54] compared the coarsening behavior of VC, TiC, and (Ti,V)C precipitates in ferrite and found that TiC coarsened most rapidly whereas (Ti,V)C coarsened slowest, ascribing this to the high chemical-bonding energy of the (Ti,V)C precipitates.

For precipitates with two or more micro-alloying elements, their chemical composition not only depends on the initial elemental concentration in steel, but also varies with its size (as shown in Fig. 4e). Atomic fraction of Ti increases in (Ti,W)C precipitates [40], but decreases in (Ti,Nb)C precipitates [55] and (Ti,Nb)(C,N) precipitates [56]. The evolution of the atomic fraction of Ti in (Ti,Mo)C precipitates is controversial: an increase was reported in [40,55] whereas a decrease was reported in [28] with increasing precipitates size. Variations in precipitate composition lead to differences in precipitate lattice parameter. This explains why different lattice parameters values have been reported for multi-component precipitates, for instance, 0.445 nm in [21] whereas 0.438 nm in [22] for (Ti,Nb)C precipitates, and 0.433 nm in [23] whereas 0.423–0.430 nm in [24] for (Ti,Mo)C precipitates.

4.3. Hardness evolution

Normally, hardness decreases when annealing a cold-rolled steel mainly due to recrystallization. Yet, for our samples, the hardness was observed to first increase and then decrease when annealing at both two temperatures. This hardness evolution is a combined result of precipitation, recrystallization and grain growth. Fig. 11 shows a schematic illustration of the hardness evolution. Three different stages in time can be discerned:

Stage I: Up to 6 min at 650 °C and 1 min at 700 °C where peak hardness occurs. Within this stage precipitation hardening occurs, while recrystallization has not yet started (but recovery occurs). Interestingly, the annealing time corresponding to the peak in hardness coincides with the time where the SANS signal shown in Fig. 7a and b shows a clear minimum for $Q < 0.15\ nm^{-1}$. This is probably related to the decrease in dislocation density (due to recovery). It is inferred that disappeared dislocations are mainly statistically stored dislocations, which do not contribute to dislocation hardening [57]. At the same time small precipitates grow as deduced from the TEM results. This is consistent with the increase in the SANS intensity for $Q > 0.15\ nm^{-1}$. The overall hardness increase observed thus shows that precipitation hardening is dominant.

Stage II: From 6 min to 8 h at 650 °C and from 1 min to 30 min at 700 °C as estimated from the VLM images (see Fig. 2). During this stage, the dislocation density decreases rapidly. Hardness decrease caused by recrystallization is dominant compared with precipitation hardening. Therefore, the hardness decreases dramatically.

Stage III: From 30 min to 4 h at 700 °C. During this stage, the hardness decrease is caused by precipitate coarsening and grain growth.

5. Conclusions

Cold-rolled Ti-V HSLA steel was isothermally annealed at 650 °C and 700 °C for different times. The microstructure, precipitate and hardness evolution have been investigated and precipitates were quantitatively characterized and compared by a combination of TEM imaging, TEM-EDS, matrix dissolution and SANS measurements. The main conclusions are:

(1) Recrystallization is (nearly) complete after annealing at 650 °C for 8 h, while it takes 30 min at 700 °C.
(2) Three types of precipitates were identified in all the samples: large cuboidal Ti(C,N), medium-size ellipsoidal (Ti,V)(C,N) and small spherical (Ti,V)C. The first two types are thermodynamically stable while the third type evolves during the annealing.
(3) For (Ti,V)C precipitates, the Ti/(Ti + V) atomic ratio decreases with increasing precipitate radius. The annealing temperature, either 650 °C or 700 °C, or the annealing time has no observable effect on this ratio.
(4) For (Ti,V)C precipitates, their median size (R_m) increases, whereas the number density (N_p) decreases with increasing annealing time.
(5) The matrix dissolution method allowed the separate volume fraction determination of the three types of precipitates present in the CR and annealed samples, whereas only the volume fractions of (Ti,V)C precipitates were obtained from the SANS measurements for the annealed samples. The volume fraction of (Ti,V)C precipitates obtained by both methods is in close agreement, but both provide slight underestimations.
(6) The hardness was observed to first increase and then decrease when annealing at both 650 °C and 700 °C. The initial hardness increase is dominated by precipitation whereas the subsequent large decrease is mainly caused by recrystallization.

CRediT authorship contribution statement

Xukai Zhang: Conceptualization, Investigation, Formal analysis, Writing - original draft. **Chrysoula Ioannidou:** Investigation, Formal analysis. **Gert H. ten Brink:** Investigation. **Alfonso Navarro-López:** Investigation. **Jan Wormann:** Investigation. **Jean Campaniello:** Resources. **Robert M. Dalgliesh:** Investigation. **Ad A. van Well:** Formal analysis. **S. Erik Offerman:** Writing - review & editing. **Winfried Kranendonk:** Writing - review & editing. **Bart J. Kooi:** Supervision, Writing - review & editing.

Declaration of competing interest

The authors declare that they have no known competing financial interests or personal relationships that could have appeared to influence the work reported in this paper.

Acknowledgements

This research was carried out under project number F41.5.15566 in the framework of the Partnership Program of the Materials innovation institute M2i (www.m2i.nl) and the Foundation for Fundamental Research on Matter (FOM) (www.fom.nl), which is part of the Netherlands Organization for Scientific Research (www.nwo.nl). Experiments at the ISIS Neutron and Muon Source were supported by a

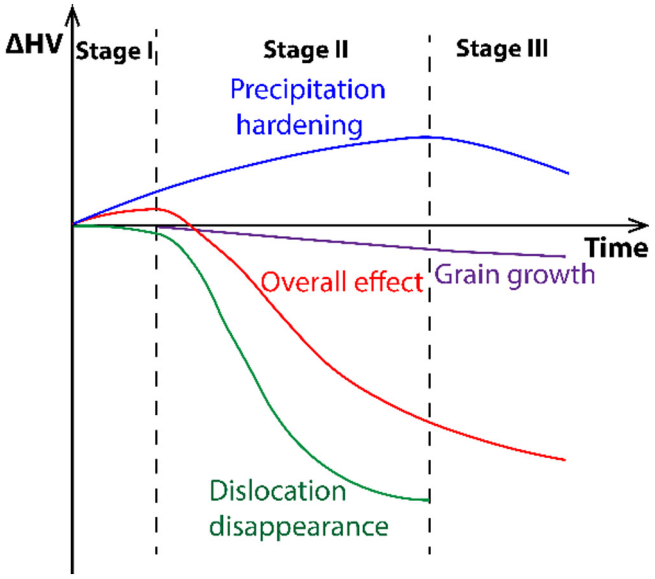

Fig. 11. Schematic illustration of the hardness evolution during annealing of the cold-rolled HSLA steel.

beamtime allocation RB1869021 [58] from the Science and Technology Facilities Council.

Appendix A. Supplementary data

Supplementary data to this article can be found online at https://doi.org/10.1016/j.matdes.2020.108720.

References

[1] E.-E. Commission, A Resource-efficient Europe-Flagship Initiative Under the Europe 2020 Strategy, Commun. (COM 21), 2011.
[2] T. Gladman, The Physical Metallurgy of Microalloyed Steels, Maney Pub, 1997.
[3] T. Taylor, P. Evans, Sensitivity of novel 460MPa proof strength titanium-vanadium microalloyed high strength low alloy steels to annealing linespeed and soak temperature, Mater. Des. 86 (2015) 714–722. https://doi.org/10.1016/j.matdes.2015.07.138.
[4] L. García-Sesma, B. López, B. Pereda, Effect of coiling conditions on the strengthening mechanisms of Nb microalloyed steels with high Ti addition levels, Mater. Sci. Eng. A 748 (2019) 386–395. https://doi.org/10.1016/J.MSEA.2019.01.105.
[5] N. Isasti, D. Jorge-Badiola, M.L. Taheri, P. Uranga, Microstructural and precipitation characterization in Nb-Mo microalloyed steels: estimation of the contributions to the strength, Met. Mater. Int. 20 (2014) 807–817. https://doi.org/10.1007/s12540-014-5002-1.
[6] S.W. Ooi, G. Fourlaris, A comparative study of precipitation effects in Ti only and Ti–V Ultra Low Carbon (ULC) strip steels, Mater. Charact. 56 (2006) 214–226, https://doi.org/10.1016/J.MATCHAR.2005.11.010.
[7] C.Y. Chen, M.H. Liao, Synergistic effects of carbon content and Ti/Mo ratio on precipitation behavior of HSLA steel: insights from experiment and critical patent analysis, Mater. Des. 186 (2020), 108361. https://doi.org/10.1016/j.matdes.2019.108361.
[8] J. Lu, O. Omotoso, J.B. Wiskel, D.G. Ivey, H. Henein, Strengthening mechanisms and their relative contributions to the yield strength of microalloyed steels, Metall. Mater. Trans. A Phys. Metall. Mater. Sci. 43 (2012) 3043–3061, https://doi.org/10.1007/s11661-012-1135-3.
[9] J.Y. Choi, B.S. Seong, S.C. Baik, H.C. Lee, Precipitation and recrystallization behavior in extra low carbon steels, ISIJ Int. 42 (2002) 889–893, https://doi.org/10.2355/isijinternational.42.889.
[10] C. Ledermueller, H.I. Pratiwi, R.F. Webster, M. Eizadjou, S.P. Ringer, S. Primig, Microalloying effects of Mo versus Cr in HSLA steels with ultrafine-grained ferrite microstructures, Mater. Des. 185 (2020), 108278. https://doi.org/10.1016/j.matdes.2019.108278.
[11] N. Prasad, S. Kumar, P. Kumar, S.N. Ojha, Mechanical properties of a cold-rolled annealed HSLA steel, J. Mater. Sci. 26 (1991) 5158–5162, https://doi.org/10.1007/BF01143207.
[12] E.M.M. Janošec, I. Schindler, V. Vodárek, J. Palát, S. Rusz, P. Suchánek, M. Růžička, Microstructure and mechanical properties of cold rolled, annealed HSLA strip steels, Arch. Civ. Mech. Eng. 7 (2007) 29–38, https://doi.org/10.1016/S1644-9665(12)60208-8.
[13] Z. Liu, R.O. Olivares, Y. Lei, C.I. Garcia, G. Wang, Microstructural characterization and recrystallization kinetics modeling of annealing cold-rolled vanadium microalloyed HSLA steels, J. Alloys Compd. 679 (2016) 293–301, https://doi.org/10.1016/j.jallcom.2016.04.057.
[14] K. Mukunthan, E.B. Hawbolt, Modeling recovery and recrystallization kinetics in cold-rolled Ti-Nb stabilized interstitial-free steel, Metall. Mater. Trans. A Phys. Metall. Mater. Sci. 27 (1996) 3410–3423, https://doi.org/10.1007/BF02595434.
[15] I. Kapoor, Y. Lan, A. Rijkenberg, Z. Li, V. Janik, Quasi in-situ analysis of geometrically necessary dislocation density in α-fibre and γ-fibre during static recrystallization in cold-rolled low-carbon Ti-V bearing microalloyed steel, Mater. Charact. 145 (2018) 686–696, https://doi.org/10.1016/J.MATCHAR.2018.09.032.
[16] C. Fang, C.I. Garcia, S.H. Choi, A.J. DeArdo, A study of the batch annealing of cold-rolled HSLA steels containing niobium or titanium, Metall. Mater. Trans. A Phys. Metall. Mater. Sci. 46 (2015) 3635–3645, https://doi.org/10.1007/s11661-015-2949-6.
[17] A. Belyakov, F.G. Wei, K. Tsuzaki, Y. Kimura, Y. Mishima, Incomplete recrystallization in cold worked steel containing TiC, Mater. Sci. Eng. A 471 (2007) 50–56, https://doi.org/10.1016/j.msea.2007.04.022.
[18] F. Perrard, C. Scott, Vanadium precipitation during intercritical annealing in cold rolled TRIP steels, ISIJ Int. 47 (2007) 1168–1177, https://doi.org/10.2355/isijinternational.47.1168.
[19] W. Al-Shalfan, J.G. Speer, D.K. Matlock, K. Findley, Effect of annealing time on solute carbon in ultralow-carbon Ti-V and Ti-Nb steels, Metall. Mater. Trans. A. 37 (2006) 207–216, https://doi.org/10.1007/s11661-006-0165-0.
[20] J. Chen, M. Lü, S. Tang, Z. Liu, G. Wang, Microstructure, mechanical properties and interphase precipitation behaviors in V-Ti microalloyed steel, Jinshu Xuebao/Acta Metall. Sin. 50 (2014) 524–530, https://doi.org/10.3724/SP.J.1037.2013.00681.
[21] S.G. Hong, K.B. Kang, C.G. Park, Strain-induced precipitation of NbC in Nb and Nb-Ti microalloyed HSLA steels, Scr. Mater. 46 (2002) 163–168, https://doi.org/10.1016/S1359-6462(01)01214-3.
[22] F.Z. Bu, X.M. Wang, S.W. Yang, C.J. Shang, R.D.K. Misra, Contribution of interphase precipitation on yield strength in thermomechanically simulated Ti-Nb and Ti-Nb-Mo microalloyed steels, Mater. Sci. Eng. A 620 (2015) 22–29, https://doi.org/10.1016/j.msea.2014.09.111.
[23] Y. Funakawa, T. Shiozaki, K. Tomita, T. Yamamoto, E. Maeda, Development of high strength hot-rolled sheet steel consisting of ferrite and nanometer-sized carbides, ISIJ Int. 44 (2004) 1945–1951, https://doi.org/10.2355/isijinternational.44.1945.
[24] H.W. Yen, C.Y. Huang, J.R. Yang, Characterization of interphase-precipitated nanometer-sized carbides in a Ti-Mo-bearing steel, Scr. Mater. 61 (2009) 616–619, https://doi.org/10.1016/j.scriptamat.2009.05.036.
[25] I. Timokhina, M.K. Miller, J. Wang, H. Beladi, P. Cizek, P.D. Hodgson, On the Ti-Mo-Fe-C atomic clustering during interphase precipitation in the Ti-Mo steel studied by advanced microscopic techniques, Mater. Des. 111 (2016) 222–229, https://doi.org/10.1016/j.matdes.2016.08.086.
[26] C. Ioannidou, Z. Arechabaleta, A. Navarro-López, A. Rijkenberg, R.M. Dalgliesh, S. Kölling, V. Bliznuk, C. Pappas, J. Sietsma, A.A. van Well, S.E. Offerman, Interaction of precipitation with austenite-to-ferrite phase transformation in vanadium micro-alloyed steels, Acta Mater. 181 (2019) 10–24, https://doi.org/10.1016/j.actamat.2019.09.046.
[27] Y.Q. Wang, S.J. Clark, V. Janik, R.K. Heenan, D.A. Venero, K. Yan, D.G. McCartney, S. Sridhar, P.D. Lee, Investigating nano-precipitation in a V-containing HSLA steel using small angle neutron scattering, Acta Mater. 145 (2018) 84–96, https://doi.org/10.1016/J.ACTAMAT.2017.11.032.
[28] S. Dhara, R.K.W. Marceau, K. Wood, T. Dorin, I.B. Timokhina, P.D. Hodgson, Precipitation and clustering in a Ti-Mo steel investigated using atom probe tomography and small-angle neutron scattering, Mater. Sci. Eng. A 718 (2018) 74–86, https://doi.org/10.1016/j.msea.2018.01.070.
[29] F. Perrard, A. Deschamps, F. Bley, P. Donnadieu, P. Maugis, IUCr, a small-angle neutron scattering study of fine-scale NbC precipitation kinetics in the α-Fe–Nb–C system, J. Appl. Crystallogr. 39 (2006) 473–482, https://doi.org/10.1107/S002188980601301X.
[30] A. Deschamps, F. Danoix, F. De Geuser, T. Epicier, H. Leitner, M. Perez, Low temperature precipitation kinetics of niobium nitride platelets in Fe, Mater. Lett. 65 (2011) 2265–2268, https://doi.org/10.1016/J.MATLET.2011.03.110.
[31] F.L. Alcântara, R. Barbosa, M.A. Cunha, Study of aluminum nitride precipitation in Fe-3%Si steel, Mater. Res. 16 (2013) 1039–1044, https://doi.org/10.1590/s1516-14392013005000090.
[32] J. Lu, J.B. Wiskel, O. Omotoso, H. Henein, D.G. Ivey, Matrix dissolution techniques applied to extract and quantify precipitates from a microalloyed steel, Metall. Mater. Trans. A Phys. Metall. Mater. Sci. 42 (2011) 1767–1784, https://doi.org/10.1007/s11661-010-0579-6.
[33] A. Hegetschweiler, T. Staudt, T. Kraus, An improved method for the matrix dissolution extraction of nanoparticles from microalloyed steel, J. Mater. Sci. 54 (2019) 5813–5824, https://doi.org/10.1007/s10853-018-03263-0.
[34] Y. Ishiguro, K. Sato, T. Murayama, Precipitation of copper sulfide in ultra low carbon steel containing residual level of copper, Mater. Trans. 46 (2005) 769–778, https://doi.org/10.2320/matertrans.46.769.
[35] A.L. Rivas, E. Vidal, D.K. Matlock, J.G. Speer, Electrochemical extraction of microalloy carbides in Nb-steel, Rev. Metal. 44 (2008) 447–456, https://doi.org/10.3989/revmetalm.0771.
[36] C.G. Windsor, An Introduction to Small-angle Neutron Scattering, 21.21, 1988 582–588, https://doi.org/10.1107/S0021889888008404.
[37] B.S. Seong, E. Shin, S.-H. Choi, Y. Choi, Y.S. Han, K.H. Lee, Y. Tomota, Quantitative analysis of fine nano-sized precipitates in low-carbon steels by small angle neutron scattering, Appl. Phys. A Mater. Sci. Process. 99 (2010) 613–620, https://doi.org/10.1007/s00339-010-5630-3.
[38] C.P. Reip, S. Shanmugam, R.D.K. Misra, High strength microalloyed CMn (V–Nb–Ti) and CMn(V–Nb) pipeline steels processed through CSP thin-slab technology: micro-

structure, precipitation and mechanical properties, Mater. Sci. Eng. A 424 (2006) 307–317, https://doi.org/10.1016/J.MSEA.2006.03.026.
[39] A. Pandit, A. Murugaiyan, A.S. Podder, A. Haldar, D. Bhattacharjee, S. Chandra, R.K. Ray, Strain induced precipitation of complex carbonitrides in Nb–V and Ti–V microalloyed steels, Scr. Mater. 53 (2005) 1309–1314, https://doi.org/10.1016/J.SCRIPTAMAT.2005.07.003.
[40] J.H. Jang, C.-H. Lee, Y.-U. Heo, D.-W. Suh, Stability of (Ti, M)C (M = Nb, V, Mo and W) carbide in steels using first-principles calculations, Acta Mater. 60 (2012) 208–217, https://doi.org/10.1016/J.ACTAMAT.2011.09.051.
[41] S.M. He, N.H. Van Dijk, M. Paladugu, H. Schut, J. Kohlbrecher, F.D. Tichelaar, S. Van Der Zwaag, In situ determination of aging precipitation in deformed Fe-Cu and Fe-Cu-B-N alloys by time-resolved small-angle neutron scattering, Phys. Rev. B-Condens. Matter Mater. Phys. 82 (2010) https://doi.org/10.1103/PhysRevB.82.174111.
[42] S. Zhang, J. Kohlbrecher, F.D. Tichelaar, G. Langelaan, E. Brück, S. van der Zwaag, N.H. van Dijk, Defect-induced Au precipitation in Fe–Au and Fe–Au–B–N alloys studied by in situ small-angle neutron scattering, Acta Mater. 61 (2013) 7009–7019, https://doi.org/10.1016/J.ACTAMAT.2013.08.015.
[43] L.A. Feigin, D.I. Svergun, Structure Analysis by Small-angle X-Ray and Neutron Scattering, Springer US, Boston, MA, 1987https://doi.org/10.1007/978-1-4757-6624-0.
[44] G.G. Long, L.E. Levine, Ultra-small-angle X-ray scattering from dislocation structures, Acta Crystallogr. Sect. A Found. Crystallogr. 61 (2005) 557–567, https://doi.org/10.1107/S0108767305031119.
[45] E. Meslin, M. Lambrecht, M. Hernández-Mayoral, F. Bergner, L. Malerba, P. Pareige, B. Radiguet, A. Barbu, D. Gómez-Briceño, A. Ulbricht, A. Almazouzi, Characterization of neutron-irradiated ferritic model alloys and a RPV steel from combined APT, SANS, TEM and PAS analyses, J. Nucl. Mater. 406 (2010) 73–83, https://doi.org/10.1016/J.JNUCMAT.2009.12.021.
[46] A.J. Allen, D. Gavillet, J.R. Weertman, SANS and TEM studies of isothermal M2C carbide precipitation in ultrahigh strength AF1410 steels, Acta Metall. Mater. 41 (1993) 1869–1884, https://doi.org/10.1016/0956-7151(93)90207-9.
[47] J. Lu, D.G. Ivey, H. Henein, A review of methods to quantify nanoscale precipitates in microalloyed steels - part 2, Iron Steel Technol 10 (2013) 232–245.
[48] M. Saeki, F. Kurosawa, M. Matsuo, Micro and state analysis as the basis for microalloying techniques, Trans. Iron Steel Inst. Japan. 26 (2011) 1017–1035, https://doi.org/10.2355/isijinternational1966.26.1017.
[49] S.M. Vonk, Precipitates on Dislocations Mathematical Modelling of Nucleating and Growing Precipitates on Dislocations, Delft University of Technology, 2016. http://repository.tudelft.nl/.
[50] G. Greenwood, The growth of dispersed precipitates in solutions, Acta Metall. 4 (1956) 243–248, https://doi.org/10.1016/0001-6160(56)90060-8.
[51] I.M. Lifshitz, V.V. Slyozov, The kinetics of precipitation from supersaturated solid solutions, J. Phys. Chem. Solids 19 (1961) 35–50, https://doi.org/10.1016/0022-3697(61)90054-3.
[52] N.A. Gjostein, Diffusion in Metals, ASM, Westerville, OH, 1973.
[53] C.D. Versteylen, N.H. Van Dijk, M.H.F. Sluiter, First-Principles Analysis of Solute Diffusion in Dilute Bcc Fe- X Alloys, 94105, 2017 1–13, https://doi.org/10.1103/PhysRevB.96.094105.
[54] G.L. Dunlop, R.W.K. Honeycombe, Ageing characteristics of VC, TiC, and (V, Ti)C dispersions in ferrite, Met. Sci. 12 (1978) 367–371, https://doi.org/10.1179/msc.1978.12.8.367.
[55] C.Y. Chen, C.C. Chen, J.R. Yang, Microstructure characterization of nanometer carbides heterogeneous precipitation in Ti–Nb and Ti–Nb–Mo steel, Mater. Charact. 88 (2014) 69–79, https://doi.org/10.1016/J.MATCHAR.2013.11.016.
[56] H. Zou, J.S. Kirkaldy, Carbonitride precipitate growth in titanium/niobium microalloyed steels, Metall. Trans. A. 22 (1991) 1511–1524, https://doi.org/10.1007/BF02667365.
[57] D.A. Hughes, N. Hansen, D.J. Bammann, Geometrically necessary boundaries, incidental dislocation boundaries and geometrically necessary dislocations, Scr. Mater. 48 (2003) 147–153, https://doi.org/10.1016/S1359-6462(02)00358-5.
[58] B.J. Kooi, E. van der Wal, A. Navarro-López, C. Ioannidou, A.A. van Well, R.M. Dalgliesh, S.E. Offerman, Precipitate evolution in cold rolled Ti-V high strength low alloy (HSLA) steel, STFC ISIS Neutron and Muon Source, 2019https://doi.org/10.5286/ISIS.E.RB1869021.